Polarization-Resolved Broadband MoS$_2$/Black Phosphorus/MoS$_2$ Optoelectronic Memory with Ultralong Retention Time and Ultrahigh Switching Ratio

Chang Liu, Xuming Zou,* Min-Ci Wu, Yang Wang, Yawei Lv,* Xinpei Duan, Sen Zhang, Xingqiang Liu, Wen-Wei Wu, Weida Hu, Zhiyong Fan, and Lei Liao*

The rapidly emerging requirement for device miniaturization and structural flexibility make 2D semiconductors and their van der Waals (vdWs) heterostructures extremely attractive for nonvolatile optoelectronic memory (NOM) applications. Although several concepts for 2D NOM have been demonstrated, multi-heterojunction devices capable of further improving storage performance have received little attention. This work reports a concept for MoS$_2$/black phosphorus (BP)/MoS$_2$ multi-heterojunction NOM with artificial trap sites through the BP oxidation, in which the trapped holes at BP/PO$_x$ interface intrigue a persistent photoconductivity that hardly recovers within the experimental time scales (exceeding 10^4 s). As a result of the interfacial trap-controlled charge injection, the device exhibits excellent photo-responsive memory characteristics, including a record high detectivity of $\approx 1.2 \times 10^{16}$ Jones, a large light-to-dark switching ratio of $\approx 1.5 \times 10^7$, an ultralow off-state current of ≈ 1.2 pA, and an outstanding multi-bit storage capacity (11 storage states, 546 nC state^{-1}). In addition, the middle BP layer in the multi-heterojunction enables broadband spectrum distinction (375–1064 nm), together with a high polarization ratio of 8.4. The obtained results represent the significant step toward the high-density integration of optoelectronic memories with 2D vdWs heterostructures.

1. Introduction

Semiconductor memories are crucial components in the modern electronic industry.[1,2] However, with Moore's Law nearing its end, the strategy of continuously shrinking the device size to ensure that more memory cells are integrated per unit area, has been severely restricted by technology complexity and the diffraction limit.[3–5] To solve this bottleneck

challenge, an alternative strategy is to develop high-capacity multi-bit memory, where each memory cell has 2^n storage levels (typically represented by current levels).[6–8] In this regard, nonvolatile optoelectronic memory (NOM) has emerged as a promising candidate, as it allows multilevel storage operations by optical programming and electrical readout. Compared with traditional image sensors containing both photodetectors and electronic memories, the unique capability of directly responding to the optical signal can effectively simplify image capturing circuitry.[9–11] Meanwhile, the non-contact writing method allows a simpler device configuration and can effectively prohibit the vertical leakage current. More importantly, the stored data can be encrypted through a specific wavelength and polarization direction.[12] These advantages attribute NOM to be extremely attractive for confidential information recording, optical communication and logic data processing. Of these, NOMs based on 2D semiconductors and their van der Waals (vdWs) heterostructures have elicited tremendous attention due to their high absorption coefficient, tunable bandgap, structural flexibility, as well as significant photo-generated charge trapping caused by their large surface-to-volume ratio.[13–19]

In recent years, several concepts for 2D NOMs have been demonstrated. Along these lines, the graphene/MoS$_2$ vdWs heterostructure-based NOM exhibited considerable number

Dr. C. Liu, Prof. X. M. Zou, Prof. Y. W. Lv, Dr. X. P. Duan, Dr. S. Zhang, Prof. X. Q. Liu, Prof. L. Liao
Key Laboratory for Micro/Nano Optoelectronic Devices of Ministry of Education & Hunan Provincial Key Laboratory of Low-Dimensional Structural Physics and Devices
School of Physics and Electronics
Hunan University
Changsha 410082, China
E-mail: zouxuming@hnu.edu.cn; lvyawei@hnu.edu.cn; liaolei@whu.edu.cn

Dr. M.-C. Wu, Prof. W.-W. Wu
Department of Materials Science and Engineering
National Chiao Tung University
Hsinchu 300, Taiwan

Dr. Y. Wang, Prof. W. D. Hu
State Key Laboratory of Infrared Physics
Shanghai Institute of Technical Physics
Chinese Academy of Sciences
Shanghai 200083, China

Prof. Z. Y. Fan
Department of Electronic and Computer Engineering
The Hong Kong University of Science and Technology
Clear Water Bay, Kowloon, Hong Kong SAR, China

of photo-responsive properties by combining MoS_2 conductive channel with graphene light absorption layer.[1] However, the low current switching ratio (I_{light}/I_{dark}, where I_{light} and I_{dark} denote the output current with and without light illumination, respectively) of <10 derived from the high dark current of graphene hinders its multi-bit storage application. Although NOM based on MoS_2/carbon nanotubes heterostructure showed an improved switching ratio of 10^5, it had only a short retention time of <10^3 s due to the limited lifetime of localized carriers at the heterojunction interface.[13] In addition, the MoS_2/PbS heterostructure was employed to store the infrared signals, while suffering from ultralow switching ratio of <10 and short retention time of 10^3 s.[11] Besides the NOMs fabricated by 2D heterostructures, single MoS_2 device has made a giant leap in retention time up to 10^4 s by introducing artificial charge traps at SiO_2/MoS_2 interface,[15] yet the data storage capacity remained limited for practical application due to the moderate switching ratio of 10^3. The above reports have made great progress in unilateral performance improvement, but to date, there is no report that could achieve a breakthrough in the overall performance of the device, especially in terms of multi-bit storage capacity, long data retention time, and the ability of broadband spectrum distinction.

Here, we demonstrate a new route for the fabrication of polarization-resolved broadband NOM that provides an ultralong retention time while retaining an ultrahigh switching ratio. The light-modulated memory capability is achieved by exploiting black phosphorus (BP) oxidation induced defects in vertically-stacked MoS_2/BP/MoS_2 layers. Under illumination, the photo-generated carriers within the heterojunction are spatially separated caused by the built-in potential. The type-II vdWs hetero-interface leads to electron transfer from BP to MoS_2, leaving confined holes in BP that induces photoconductive gain as electron recirculates in the channel. In this device architecture, we utilize low noise of photodiode and high gain of photoconductor to obtain an ultrahigh switching ratio of 1.5×10^7 together with a record high detectivity of 1.2×10^{16} Jones, while massive in-gap defect states introduced by the BP oxidation are responsible for the ultralong retention time exceeding 6×10^4 s. More importantly, through this unique device design, our device has obtained high multi-bit storage performance (11 storage states, 546 nC state^{-1}) as well as polarization and broadband spectrum resolution capabilities, evidently demonstrating its promising potency for high-performance data storage.

2. Results and Discussions

Figure 1a shows the schematic diagram of our MoS_2/BP/MoS_2 optoelectronic memory. The device architecture comprises a BP layer sandwiched between two MoS_2 layers, in which the upper surface of BP is oxidized by ozone treatment. The straightforward fabrication procedures are schematically illustrated in Figure S1 (Supporting Information). Raman spectra measured at the heterojunction region contains the peaks from BP and MoS_2 simultaneously, indicating that the MoS_2/BP/MoS_2 heterostructure is coupled strongly (Figure S2, Supporting Information). Meanwhile, a significant photoluminescence (PL) quenching can be observed in the MoS_2/BP/MoS_2 heterojunction region (Figure S3, Supporting Information). The PL intensity of heterostructure region decreases by 82% compared with that of top and bottom MoS_2, which is derived from the exciton dissociation and interlayer charge transfer in hetero-interface. Figure 1b exhibits the corresponding cross-sectional high-resolution transmission electron microscopy (HRTEM) image of MoS_2/BP/MoS_2 stack, which demonstrates that ozone treatment of BP produces an amorphous phosphorus oxide (PO$_x$) of
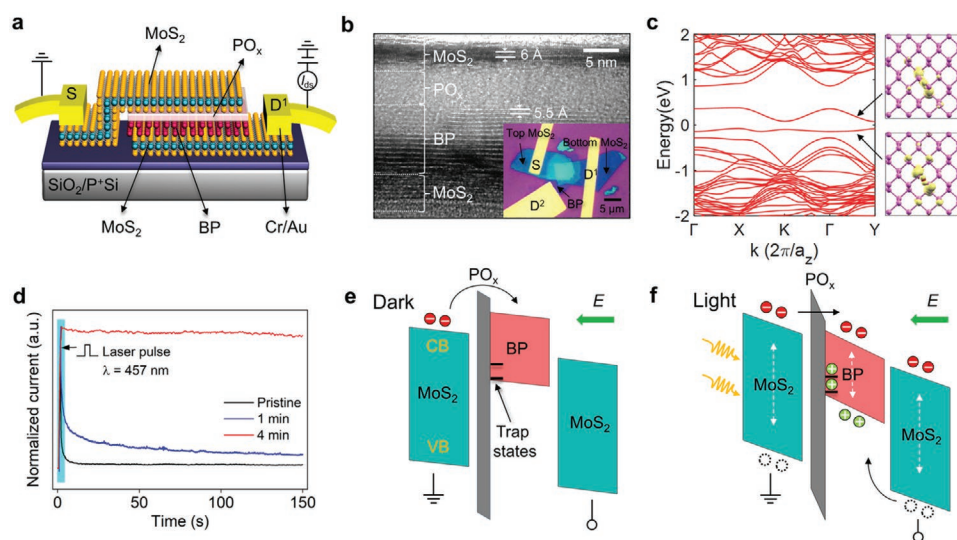

Figure 1. The structure and band diagram of MoS_2/BP/MoS_2 multi-heterojunction memory. a) Schematic structure of the MoS_2/BP/MoS_2 multi-heterojunction phototransistor. b) The high-resolution transmission electron microscopy (HRTEM) image of MoS_2/BP/MoS_2 multi-heterojunction. Inset: optical image of the corresponding device. c) The calculated band structure of oxidized phosphorene based on density functional theory (DFT). d) The photo-response memory characteristics of different ozone treatment time. e,f) Band diagram and photocarriers transfer of the multi-heterojunction device in the e) dark and f) light. Here, VB and CB denote the valence band and conduction band, respectively, and the "*E*" arrow denotes the bias electric field direction.

**ADVANCED
SCIENCE NEWS**
www.advancedsciencenews.com

**ADVANCED
FUNCTIONAL
MATERIALS**
www.afm-journal.de

≈4 nm on the upper surface of BP flake. Here, we choose 3–4 nm MoS$_2$ and 10–13 nm BP flakes because the materials with this thickness can absorb light efficiently while maintaining reasonably high mobility and large current on/off ratio for transistor operation. The optical image of a typical MoS$_2$/BP/MoS$_2$ NOM is shown in Figure 1b inset, where the three Cr/Au (10/50 nm) electrodes are defined as source (S) on the upper MoS$_2$ flake, drain 1 (D^1) on the lower MoS$_2$ flake, and drain 2 (D^2) on the BP layer, respectively. While defects in bulk semiconductors are usually considered as problematic, the defect engineering has been proved to be an effective pathway to introduce new functionalities in 2D semiconductors.[20,21] In several recent studies on BP oxidation, oxygen was reported to naturally dissociate in BP, inducing a reduction in BP layers.[22,23] According to density functional theory (DFT) calculation (Figure 1c), the incorporation of oxygen would induce in-gap deep levels. The most favorable oxygen position adsorbed on the surface of the phosphorene generates a diagonal bridge with a P-P bond.[24] The adsorption energy E_b is 4.19 eV, in which the E_b is defined as $E_{ox} - (E_p + E_o)$, where E_{ox}, E_p, and E_o are the total energies of the oxidized phosphorene, the pristine phosphorene, and the O atom, respectively. The two deep levels located around the oxygen defect as shown in the real-space density of states isosurfaces on the right panel, indicating their excellent carrier trapping ability. To validate this hypothesis, the hysteretic behaviors of BP field-effect transistor are characterized on the basis of ozone treatment time (Figure S4, Supporting Information). Here, the hysteresis window increases with the ozone treatment time so that the trapped carrier density increases simultaneously. It is clearly confirmed that the ozone treatment induces charge trap sites in BP, which are expected to generate a high photoconductivity gain in our device architecture. As shown in Figure 1d, the MoS$_2$/BP/MoS$_2$ optoelectronic memories with different ozone treatment times are fed with 457 nm laser pulse at $V_{ds} = 1$ V, $V_{gs} = 0$ V, and an incident laser power density (P_{light}) of 40 mW cm^{-2}. After treating the upper surface of BP for 4 min, the corresponding device exhibited a remarkable light-induced memory behavior via the steady persistent photoconductivity (PPC), in which the long-live charge traps govern the electron-hole recombination. In sharp contrast, the device without the ozone treatment is found to exhibit much weaker PPC characteristics. Meanwhile, the photocurrent mapping related to the optical photographs (Figure S5, Supporting Information) ensures that the photo-response of our devices is mainly induced by the multi-heterojunction.

Specifically, the presented devices work as follows. When a S-D^1 forward bias is applied without light illumination, the current is limited by the PO$_x$-induced large electron-injection barrier, as illustrated in the energy band diagram (Figure 1e). The detailed energy levels of the MoS$_2$ and BP calculated with density functional theory are shown in Figure S6 in the Supporting Information. Upon light illumination, the electron-hole pairs generated in both MoS$_2$ and BP are separated by p-n junction interfacial electric field (Figure 1f). While electrons are transported in MoS$_2$/BP/MoS$_2$ heterostructural conducting channel under the applied forward bias, holes remain trapped at BP/PO$_x$ interface due to the oxidation induced localized trap sites and large hole-injection barrier. The trapped holes quickly rise the Fermi level of BP, providing photo-gating effect as the

electrons are recirculating in the channel. The electron-injection barrier on the PO$_x$ side thus becomes so thin that more electrons would tunnel through it under a small forward bias. Therefore, the PO$_x$ layer works as an optoelectronics "valve" for electron injection, and incident photon can act as the switching trigger.

The strong photogating effect can be demonstrated by the photo-response characteristics of the device in the transfer curves (I_{ds}–V_{gs}), as shown in **Figure 2**a. Here, even at an ultralow P_{light} value of 0.6 µW cm^{-2}, we can still observe a significant threshold voltage shift (ΔV_{th}) of 15.5 V toward the negative direction. This shift can be attributed the trapping of photo-generated holes at BP/PO$_x$ interface, which can modulate the barrier height to induce the pronounced photogating effect. Using a simple parallel plate capacitor model, the trapped charges are estimated with the equation[25]

$$\Delta n = \frac{C_{ox}\,\Delta V_{th}}{q} \tag{1}$$

where C_{ox} denotes the gate capacitance (11.5 nF cm^{-2} for 300 nm SiO$_2$) and q denotes the elementary charge. Here, the doping level is calculated to be 1.1×10^{12} cm^{-2} at $P_{light} = 0.6$ µW cm^{-2}. The photo-response performance of the device is quantitatively assessed with responsivity (R), which is employed to quantify photocurrent ($I_{ph} = I_{light} - I_{dark}$) generated on active area of the device and given by[25,26]

$$R = \frac{I_{ph}}{P_{light}\,S} \tag{2}$$

Here, S refers to the overlapping area of the multi-heterojunction. As shown in Figure 2b, the photocurrent can be modulated by varying the carrier densities through electrostatic gating. The maximum R value is calculated to be 1.3×10^7 A W^{-1} at $V_{gs} = -8$ V. This value is six orders of magnitude higher than the reported MoS$_2$/BP heterojunction device[27], indicating outstanding photoresponse obtained in our MoS$_2$/BP/MoS$_2$ device. Here, the R value gradually decreases with the P_{light} value, which can be understood with the increasing recombination rate of photo-generated carriers at stronger light illumination. In addition responsivity, the light-dark current ratio of the device is an important parameter related to NOM storage capacity. Our device exhibits a maximum I_{light}/I_{dark} value of 1.5×10^7 at $V_{gs} = -75$ V and $P_{light} = 501$ mW cm^{-2} (Figure 2c). Such a high value can be attributed to the ultralow dark current (1.2 pA) in off-state of the device, as well as the amplified photocurrent caused by the photogating effect. In order to verify the above-mentioned photo-response mechanism, the photocurrent as a function of P_{light} under different V_{gs} is fitted according to the power function of $I_{ph} \propto P_{light}^{\alpha}$. Here, α is a constant. Normally, $\alpha = 1$ represents a complete photoconductive effect and $\alpha < 1$ refers to the existence of photogating effect. As shown in Figure 2d with varying V_{gs} (–75, 0 and 40 V), all the extracted α values are far less than 1, which indicates that a profound photogating effect exists in our device. We can also observe that the α value varies with V_{gs}, and it reaches a minimum of 0.08 at $V_{gs} = -5$ V (Inset of Figure 2d. This result is consistent with the photo-responsivity of our device, indicating that the
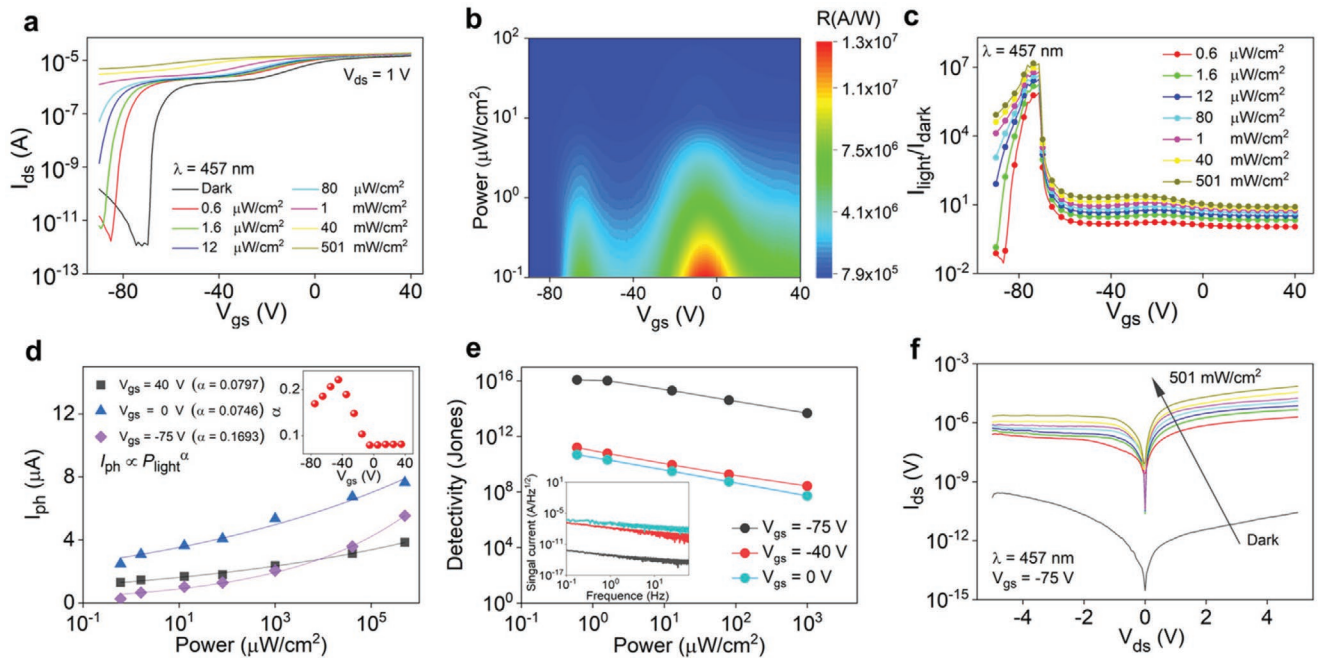
Figure 2. Optoelectronic characteristics of the $MoS_2/BP/MoS_2$ multi-heterojunction memory. a) I_{ds}–V_{gs} curves of $MoS_2/BP/MoS_2$ phototransistor under different light power density at $V_{ds} = 1$ V. b) V_{gs} and P_{light} dependent responsivity extracted from the transfer characteristic curves shown in (a). c) The extracted I_{light}/I_{dark} values with different gate voltage. d) The photocurrent plotted as a function of laser power density. Inset: the extracted exponent α for different V_{gs} values. e) Specific detectivity as a function of light power density under different gate voltage. Inset: Noise analysis of the device extracted from the Fourier transform of the dark current. f) The corresponding I_{ds}–V_{ds} curves under different light power density at $V_{gs} = -75$ V.

photogating effect is the dominant photoresponse mechanism. In addition to the responsivity and light-to-dark ratio, another important parameter is the specific detectivity (D^*), which characterizes the ability of optoelectronic devices to detect weak light signals. The D^* value is given by[12,28,29]

$$D^* = \frac{(SB)^{1/2}}{NEP} \tag{3}$$

$$NEP = \frac{\overline{i_n^2}^{1/2}}{R} \tag{4}$$

where the B, NEP and $\overline{i_n^2}^{1/2}$ is the bandwidth, the noise equivalent power, and the root-mean-square value of the noise current, respectively. The noise level per unit bandwidth (1 Hz) of the device are measured to be 7.4×10^{-15}, 1.8×10^{-8} and 2.6×10^{-7} A/Hz$^{1/2}$ under the gate voltage of -75, -40 and 0, respectively (Inset of Figure 2e). Despite the moderate responsivity value of 1.3×10^6 A W^{-1} at $V_{gs} = -75$ V, the corresponding detectivity reaches its maximum value of 1.2×10^{16} Jones arising from the suppressed noise at such low dark current (Figure 2e). This value is four orders of magnitude higher than the conventional silicon-based detectors[30,31], which clearly demonstrates that the device architecture presented here is highly sensitive to weak optical input signals. The corresponding output curves (I_{ds}–V_{ds}) at $V_{gs} = -75$ V are shown in Figure 2f. Our multi-heterojunction NOM shows an apparent transition in device operation from photodiode with rectification characteristic in the dark, to photoconductor with ultrathin electron barrier under light illumination, thereby combining low dark current and high

responsivity simultaneously. Notably, we also characterize the photo-response performance of the MoS_2/BP mono-heterojunction device under S-D^2 forward bias of 1 V, which exhibits a much lower responsivity due to the resistive lateral BP channel after ozone treatment (Figure S7, Supporting Information). Apart from that, the synergy of MoS_2 and BP also enables our device to be sensitive to near-infrared light. Figure S8 in the Supporting Information shows the photoresponse characteristics of the device upon 1064 nm illumination, which exhibits a maximum infrared responsivity of 7.6×10^3 A W^{-1}.

To explore the feasibility of $MoS_2/BP/MoS_2$ multi-heterojunction in optoelectronic memories, the device is written by a 457 nm pulsed laser at $V_{gs} = -75$ V with a duration time of 10 s and P_{light} of 501 mW cm^{-2} (**Figure 3**a). When the laser is turned on, the I_{ds} sharply increases to the finite value (I^{on}), leading a high I_{light}/I_{dark} calue of 1.5×10^7. After the pulsed laser is turned off, the initial I^{on} value of 6.0×10^{-6} A can effectively retain 86.7% within the experimental time of 6×10^4 s (Inset of Figure 3a. Table S1 presents the comparative performance metrics of various 2D NOM. It is evident that the present device performs much better than those of previously reports.

Figure 3b shows the writing/erasing process of our memory, in which the four operations, including off-state reading (1), optical writing (2), on-state reading (3), and electrical erasing (4), are displayed. For the optical writing, the I_{ds} increases rapidly to achieve a high conductive state by applying a 457 nm laser pulse (40 mW cm^{-2}, 350 ms). Subsequently, the high conductive state can be effectively maintained for on-state current reading. For electrical erasing, by applying a gate pulse (+80 V, 20 ms), the readout current initially shows a sharp increase due
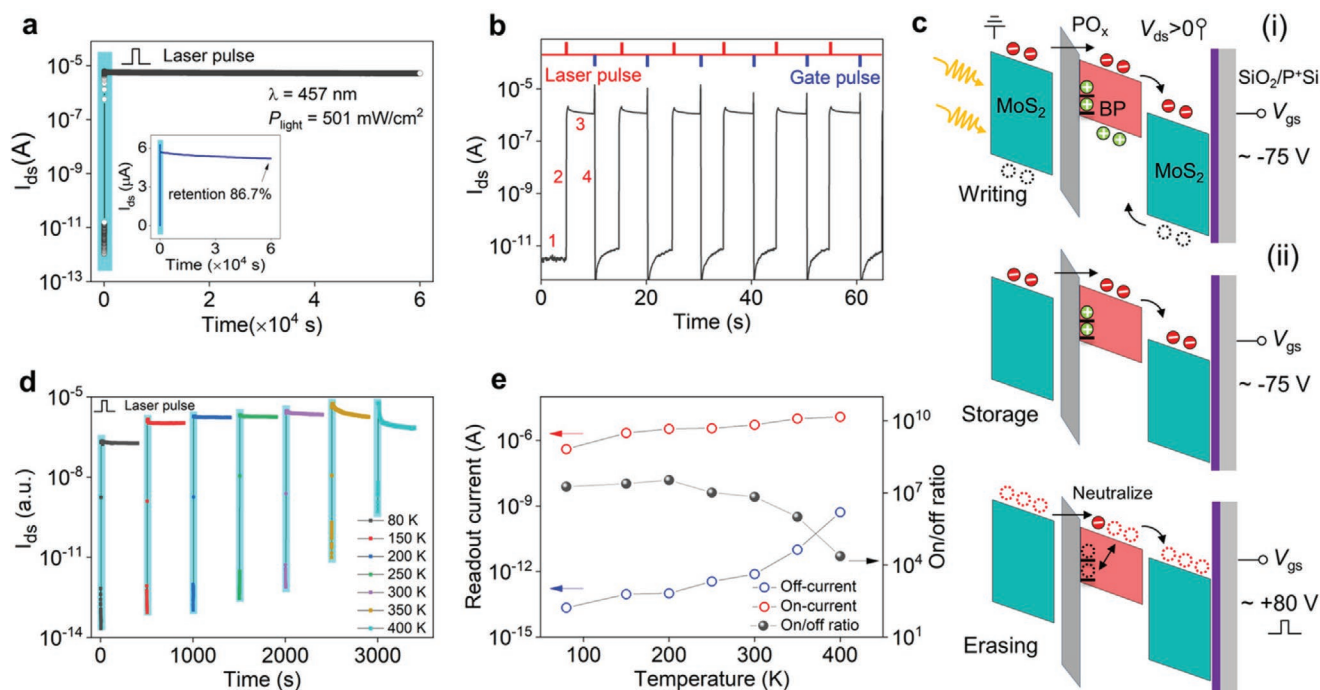
**ADVANCED
SCIENCE NEWS**

www.advancedsciencenews.com

**ADVANCED
FUNCTIONAL
MATERIALS**

www.afm-journal.de

Figure 3. Operational mechanism and temperature-dependent characteristic of MoS$_2$/BP/MoS$_2$ optoelectronic memory. a) Time evolution of I_{ds} written by a 457 nm laser pulse with P_{light} of 501 mW cm^{-2} for 10 s. Inset: I_{ds} value in linear scales. b) Writing and erasing operation of the device using laser and gate bias pulses, respectively. c) Schematic illustration of the i) writing, ii) storage, and iii) erasing process. d) Memory characteristics with different temperature (80–400 K). The retention time recorded for 400 s for each temperature and separately plotted, regardless of the initial time. e) The extracted on/off-current and ratio as a function of temperature.

to the back gate capacitance effect, and then decreases to the non-conductive initial state. Meanwhile, the device also exhibits a fast writing/erasing speed of 300/60 ms (Figure S9, Supporting Information). To explain the work mechanism of our MoS$_2$/BP/MoS$_2$ NOM, Figure 3c gives the schematic diagram of a complete operating cycle. In dark, the device is operated in off-state with the V_{gs} = –75 V. During writing process (i), the photo-generated holes are trapped in BP, leading to a high conductive state. As the laser turns off, the long-live charge traps govern the electron-hole recombination, which contributes to the ultralong PPC time, corresponding to the signal storage (ii). For erasing (iii), a positive V_{gs} (+80 V) pulse is applied. In this case, the middle BP can be converted into n-type and the trapped holes can be released via the recombination with the excess electrons.[13,32] To further explore the role of defective BP, the temperature (T)-dependent PPC was investigated with various temperatures ranging from 80 to 400 K (Figure 3d). Similarly, when the device is written by a laser pulse (10 s, 501 mW cm^{-2}), the readout current increases rapidly at all temperatures. As the temperature increases, two important features can be observed. i) The PPC relaxes as the temperature increases. This is because the trapped holes escape from the traps through thermal fluctuation.[11] ii) Both of the off-current and on-current increase slightly with the increasing temperature (Figure 3e), which is due to part of the read current contributed by the thermally excited electrons.[15] Here, even at a high temperature of 400 K, our device still has a switching ratio of 4.6×10^4, indicating that the trapped holes render robustness against thermal fluctuations. Additionally, the time-dependent I_{ds} under different V_{gs}

values are shown in Figure S10 in the Supporting Information. Under negative gate voltage, the device exhibits excellent storage characteristics. However, as the V_{gs} is close to 0 V, the device has almost no switching ratio due to the large dark current in on-state. In our work, the optoelectronic measurements are performed at V_{gs} = –75 V, in which the device is operated with an ultralow dark current.

Apart from that, we further characterize the laser power-dependent memory characteristics (**Figure 4**a). With a 457 nm laser illumination for 10 s, the read-out current of the device increases with the power density. It is worth noting that our NOM can be accessed even at an ultralow power density of 6 μW cm^{-2}, which exhibits a relatively high switching ratio of 8.9×10^4 (Inset of Figure 4a. This feature highlights the high optical sensitivity of our fabricated device. Meanwhile, the photo-responsive memory characteristics under different exposure times (t_{ph}) are also investigated (Figure 4b). When a short light exposure time of 0.3 s was applied, the significant photo-responsive memory feature with a switching ratio of 1.1×10^5 is observed, which indicates that our NOM can be effectively written with a small exposure dosage. In addition, the readout charges under different t_{ph} values are shown in Figure 4c. Intriguingly, when the exposure time is less than 10 s, the collected readout charge (Q_{ro}) is linearly dependent on the exposure time (Inset of Figure 4c), which satisfies a perfect power function formula of $Q_{ro} \approx t_{ph}^a$. The fitted result ($a = 0.99$) shows that our NOM is strictly proportional to the number of incident photons, which is beneficial for image sensor applications.[15] According to the on-off ratio of readout charge, the
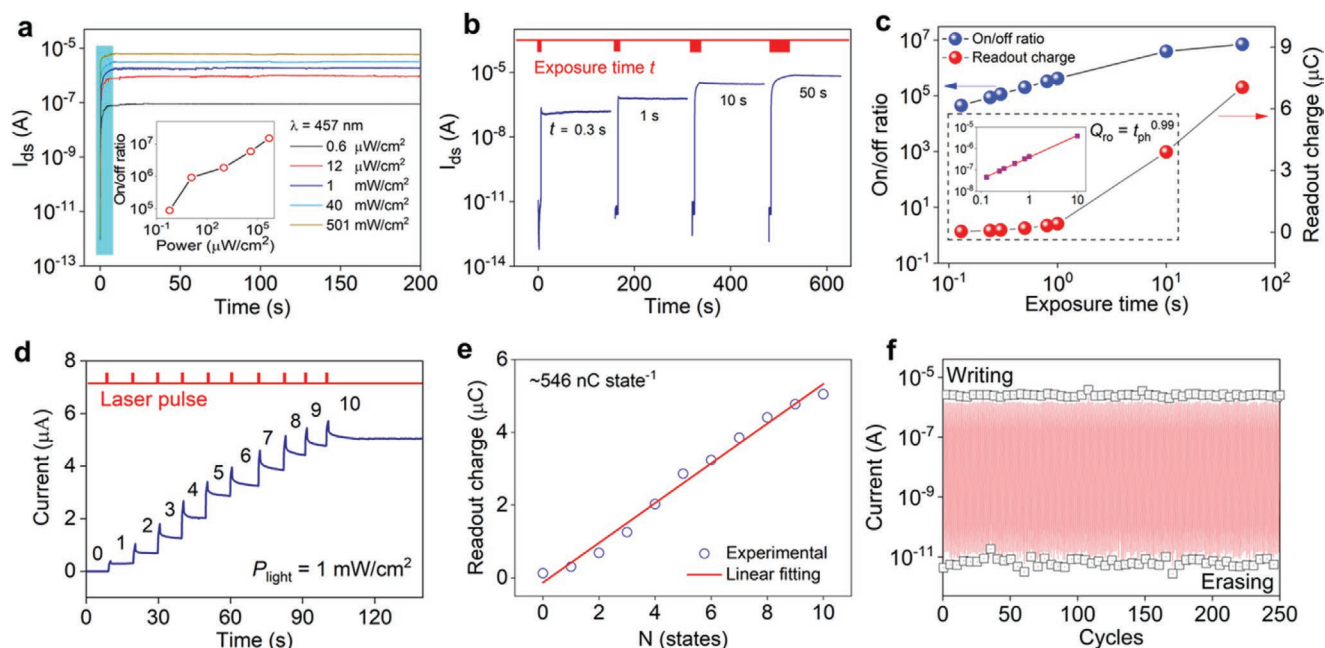
**ADVANCED
SCIENCE NEWS**
www.advancedsciencenews.com

**ADVANCED
FUNCTIONAL
MATERIALS**
www.afm-journal.de

Figure 4. Photo-response characteristics under different writing conditions, multi-bit memory and endurance performance. a) Time-dependent I_{ds} at different P_{light} value with the pulse duration time of 10 s. Inset: the extracted on/off ratio as a function of P_{light}. b) Time-dependent I_{ds} under different exposure times. The P_{light} is fixed at 1 mW cm^{-2}. c) The extracted on/off ratio (in log scale) and readout charge (in linear scale) as a function of exposure times. Inset: the linear fitting of readout charge (integrating time: 10 s). d) Readout current as a function of the number of applied laser pulses. The P_{light} and duration is 1 mW cm^{-2} and 800 ms, respectively. e) The linear fitting of collected readout current related to (d). f) Endurance of writing/erasing operation. The laser wavelength and source-drain voltage is controlled at 457 nm and 1 V, respectively.

linear dynamic range (*LDR*), which characterizes the ratio of the full-well charge capacity to the dark charge within the linear region, can be evaluated according to the equation of $LDR = 20 \times \log(I_{light}/I_{dark})$.[15] Here, the *LDR* value was calculated to be 131.8 dB, which is much larger than commercial Si-based CCDs (60–70 dB).[33] Next, we focus on the multi-bit storage capacity of the device (Figure 4d). Even with a high laser intensity (1 mW cm^{-2}, 800 ms), the device can be operated under eleven storage states defined as "0", "1" and so on. Here, the extracted retention rate value is more than 66.9%, indicating the feasibility of our device for multi-level storage. Additionally, the collected readout charge exhibits a linear relationship with the pulse number (Figure 4e), which consistently increases by ≈546 nC for each applied laser pulse. This confirms that the multi-bit memory was reliable and reproducible with repeated switching. Figure 4f shows the off- and on-current of more than 250 cycles. Under continuous writing/erasing operation, the almost unchanged on- and off- current further confirms the stability of our MoS$_2$/BP/MoS$_2$ heterostructure for optoelectronic memories.

Although the above measurements are mainly performed under 457 nm laser illumination, the device also has the capability of broadband response. **Figure 5**a gives the memory characteristics ranging from ultraviolet (UV) to near-infrared (NIR). Here, the incident power density and writing time are fixed at 8 mW cm^{-2} and 10 s, respectively, to get a saturated readout current. Our device exhibits obvious PPC for all wavelengths (375 to 1064 nm). Here, the 375 nm incident laser shows the highest switching ratio (Figure S11, Supporting Information), which can be attributed to the higher photon energy and

co-absorption of the multi-heterostructure. The obvious I^{on} change at various wavelengths demonstrates the wavelength-resolved capability of our device, which is promising for the storage of confidential information and filter-free color image sensor.[6] Here, the programming rate (*PR*) is defined to further quantify the memory capability at different wavelengths, as following[2]

$$PR = \frac{I_{store}}{P_{light}\, S\, t_{pro}} \tag{5}$$

where I_{store} denotes the readout current, and t_{pro} denotes the time of optical program. The *PR* as a function of photon energy is plotted in Figure 5b. Obviously, a monotonically increasing PR with photon energy indicates that laser with higher photon energy (shorter wavelength) induces more photo-generated carries in our device. Moreover, the calculated *PR* value is 2.3, 9.0, 15.8 and 55.9 A W^{-1} s^{-1} at the photon energy of 1.2, 1.4, 1.5 and 1.9 eV, respectively. These values are, on average, two times higher than that of the previously reported WSe$_2$/h-BN heterostructure NOM[5], confirming excellent memory efficiency obtained in our device. Considering the polarization-dependent optical properties of BP layer, it is worth to further explore the polarization sensitivity of MoS$_2$/BP/MoS$_2$ multi-heterojunction devices. Here, the device is measured with different polarization angle under 1064 nm laser illumination (Figure 5c). Apparently, the I_{ds} as illuminated along the arm-chair direction is much larger than that of zigzag direction. The photocurrent as a function of laser power density for both polarizations exhibits in (Figure S12, Supporting Information).
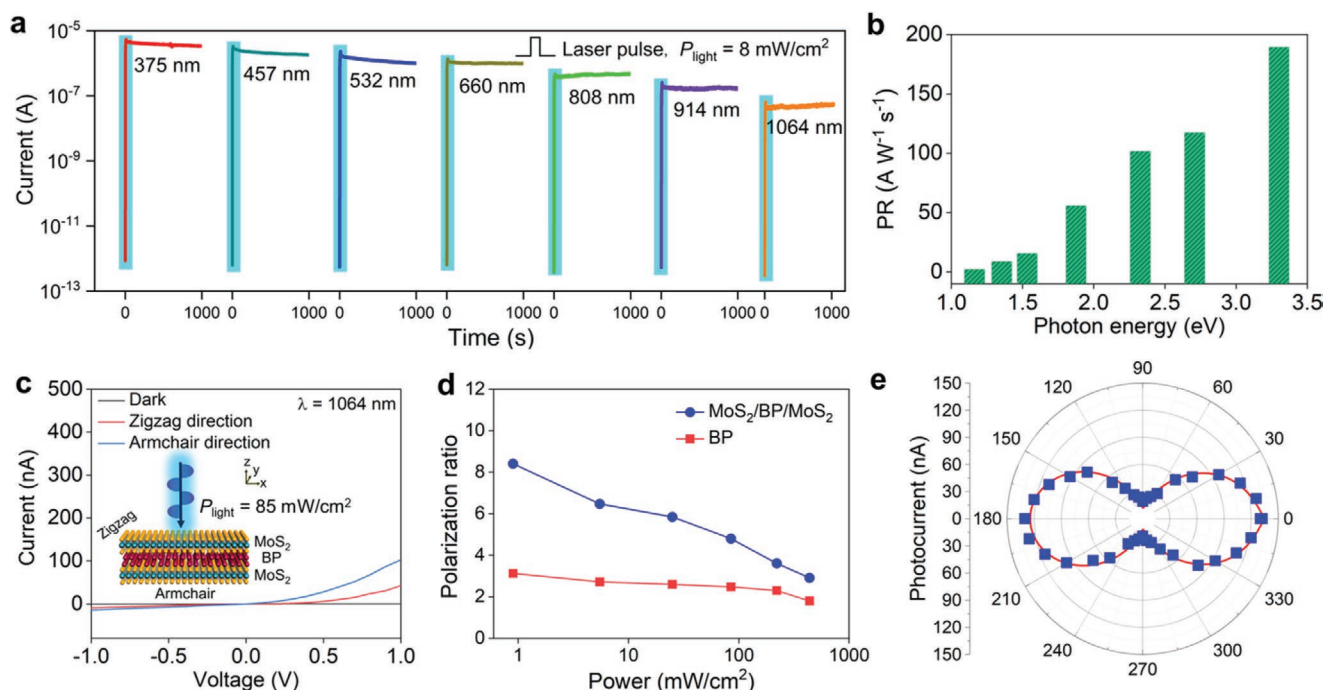
ADVANCED
SCIENCE NEWS
www.advancedsciencenews.com

ADVANCED
FUNCTIONAL
MATERIALS
www.afm-journal.de

Figure 5. Polarization-resolved broadband photo-response of the $MoS_2/BP/MoS_2$ optoelectronic memory. a) Memory behavior of the devices programmed by various wavelengths ranging from UV to NIR (375–1064 nm) region with the same light power density (P_{light} = 8 mW cm^{-2}) for 10 s. b) Programming rate as a function of incident photon energy. c) The output current versus voltage for different polarization direction under 1064 nm laser illumination (85 mW cm^{-2}). d) The extracted polarization ratio for the BP and $MoS_2/BP/MoS_2$ devices at V_{ds} = 1 V. e) The extracted photocurrent as a function of polarization angle under 1064 nm laser illumination.

The extracted polarization ratios are displayed in Figure 5d. Here, a maximum polarization ratio of 8.4 is achieved at P_{light} = 0.9 mW cm^{-2}. This ratio is 2.7 times higher than that of our fabricated single BP device, which can be attributed to the current amplification through the photogating effect in $MoS_2/BP/MoS_2$ multi-heterostructure. These results are further corroborated by the polar plot of Figure 5e. Notably, the laser-excitation direction is fixed along the armchair direction (x axis) and the data of 180 to 360° is copied from that of 0 to 180°. An obvious photocurrent variation can be observed along with the polarization angle from 0° (aligned with the x axis) to 90° (aligned with the y axis), demonstrating a desirable ability of full angle discrimination. Our polarization-resolved NOM can avoid the side-by-side configuration of polarized optics and memory devices, demonstrating a promising future for polarization information processing.

3. Conclusion

In summary, we have demonstrated a new pathway for the fabrication of polarization-resolved broadband optoelectronic memory based on $MoS_2/BP/MoS_2$ multi-heterojunction, in which the light-modulated memory capability is achieved by exploiting oxidation-induced defects in BP layer. By optimizing the $MoS_2/BP/MoS_2$ potential well structure through ozone treatment of the BP surface, the device is capable of trapping and releasing photo-generated carriers that are stored in the trap states, allowing the programmable function for memory

applications. Upon light illumination, the trapped holes at BP/PO_x interface provide profound photo-gating effect, inducing a high responsivity of 1.3×10^6 A W^{-1} and a record high detectivity up to 1.2×10^{16} Jones at V_{gs} = –75 V. In addition, the device can store the optical signal for over 6×10^4 s, together with ultrahigh light-to-dark switching ratio of 1.5×10^7, and excellent multi-bit storage capacity (11 storage states, 546 nC state^{-1}). Furthermore, we show that the device has the capability of polarization and wavelength distinction. This work clearly demonstrates the great potential of 2D vdWs multi-heterojunction devices for future data storage applications.

4. Experimental Section

Oxidation Treatment of Black Phosphorus: The few-layer BP flakes was mechanically exfoliated from a bulk crystal using Scotch tape and transferred onto a SiO$_2$/P$^+$-Si substrate. Next, the BP flakes were treated with ozone that was produced by ultraviolet light in the atmosphere conditions. After that, a self-assembly PO$_x$ layer was formed at the top of BP flakes, where the oxidation level of BP can be controlled by ozone treatment time.

Transfer Procedures and Device Fabrication: The MoS$_2$ flakes were obtained by the mechanical exfoliation, and then transferred onto the pre-cleaned P$^+$-Si substrates with a 300 nm SiO$_2$ layer. Subsequently, a pre-treated BP flake containing a PO$_x$ layer was transferred onto MoS$_2$ to form the BP/MoS$_2$ heterostructure assisted by an aligned transfer platform. The employed polymethyl methacrylate film was later washed off with acetone. Next, the similar process was performed again to transfer another MoS$_2$ flake onto the BP/MoS$_2$ sample. Notably, the top and bottom MoS$_2$ cannot contact in order to achieve desired device

architecture. Finally, the electrodes were patterned by standard electron beam lithography process, and Cr/Au (10/50 nm) electrodes were formed by thermal evaporated and standard lift-off process.

Characterization and Measurements: Raman spectrum and PL studies of all samples were conducted using a confocal Raman system (Horiba LabRAM HR) excited by a 405 nm laser. The scanning photocurrent mapping was obtained by using a scanning Galvo System (Thorlabs GVS212) equipped with a modulated laser beam. The high-resolution HRTEM image was obtained by JEOL JEM-200 F transmission electron microscope with operating at 200 kV. Electrical and photoelectrical measurements were carried out on a probe station (Lakeshore, TTP4) equipped with Agilent B1500A semiconductor parameter analyzer under vacuum condition ($\approx 1.5 \times 10^{-4}$ Pa). The light sources were lasers with wavelength of 375, 457, 532, 660, 808, 914 and 1064 nm, respectively.

First-Principles Calculation: The calculation is carried out by the open-source QUANTUM ESPRESSO plane-wave DFT package.[34] The Perdew-Burke-Ernzerhof (PBE) exchange-correlation functional with semi-empirical DFT-D3 vdWs correction method is adopted and the plane-wave cut-off energy is 585 and 666 eV for the MoS_2 and BP, respectively.[35] To avoid mirror interactions, a vacuum space of 15 Å is added between adjacent cells in the thickness direction.[36] A 4×4 phosphorene unit-cell structure is used to construct the O adsorbed phosphorene system and the Brillouin zone k-point sampling is $5 \times 5 \times 1$ for electronic ground-state computations. Before the adsorption, the crystal structures are fully relaxed until the force on each atom and total energy variations are smaller than 2.6×10^{-3} eV Å^{-1} and 1.4×10^{-3} eV.[37,38]

Supporting Information

Supporting Information is available from the Wiley Online Library or from the author.

Conflict of Interest

The authors declare no conflict of interest.

Data Availability Statement

The data that support the findings of this study are available from the corresponding author upon reasonable request.

[1] K. Roy, M. Padmanabhan, S. Goswami, T. P. Sai, G. Ramalingam, S. Raghavan, A. Ghosh, *Nat. Nanotechnol.* **2013**, *8*, 826.

[2] D. Xiang, T. Liu, J. Xu, J. Y. Tan, Z. Hu, B. Lei, Y. Zheng, J. Wu, A. H. C. Neto, L. Liu, W. Chen, *Nat. Commun.* **2018**, *9*, 2966.

[3] J. Cheng, C. Wang, X. Zou, L. Liao, *Adv. Opt. Mater.* **2019**, *7*, 1800441.

[4] J. Liu, Z. Zhang, S. Qiao, G. Fu, S. Wang, C. Pan, *Sci. Bull.* **2020**, *65*, 477.

[5] S. Zhou, B. Peng, *J. Semicond.* **2020**, *7*, 41.

[6] L. Hu, J. Yuan, Y. Ren, Y. Wang, J. Q. Yang, Y. Zhou, Y. J. Zeng, S. T. Han, S. Ruan, *Adv. Mater.* **2018**, *30*, 1801232.

[7] M. D. Tran, H. Kim, J. S. Kim, M. H. Doan, T. K. Chau, Q. A. Vu, J. H. Kim, Y. H. Lee, *Adv. Mater.* **2019**, *31*, 1807075.

[8] J. Y. Chen, Y. C. Chiu, Y. T. Li, C. C. Chueh, W. C. Chen, *Adv. Mater.* **2017**, *29*, 1702217.

[9] F. Zhou, Z. Zhou, J. Chen, T. H. Choy, J. Wang, N. Zhang, Z. Lin, S. Yu, J. Kang, H. P. Wong, Y. Chai, *Nat. Nanotechnol.* **2019**, *14*, 776.

[10] R. Cheng, F. Wang, L. Yin, Z. Wang, Y. Wen, T. A. Shifa, J. He, *Nat. Electron.* **2018**, *1*, 356.

[11] Q. Wang, W. Yao, K. Cai, R. Cheng, L. Yin, Y. Zhang, J. Li, Z. Wang, F. Wang, F. Wang, T. A. Shifa, C. Jiang, H. Yang, J. He, *Sci. Adv.* **2018**, *4*, eaap7919.

[12] J. Bullock, M. Amani, J. Cho, Y.-Z. Chen, G. H. Ahn, V. Adinolfi, V. R. Shrestha, Y. Gao, K. B. Crozier, Y.-L. Chueh, A. Javey, *Nat. Photonics* **2018**, *12*, 601.

[13] Z. Yang, H. Hong, F. Liu, Y. Liu, M. Su, H. Huang, K. Liu, X. Liang, W. J. Yu, Q. A. Vu, X. Liu, L. Liao, *Small* **2019**, *15*, 1804661.

[14] A. C. Gadelha, A. R. Cadore, K. Watanabe, T. Taniguchi, A. M. de Paula, L. M. Malard, R. G. Lacerda, L. C. Campos, *2D Mater.* **2019**, *6*, 025036.

[15] J. Lee, S. Pak, Y. W. Lee, Y. Cho, J. Hong, P. Giraud, H. S. Shin, S. M. Morris, J. I. Sohn, S. Cha, J. M. Kim, *Nat. Commun.* **2017**, *8*, 14734.

[16] W. Huang, L. Yin, F. Wang, R. Cheng, Z. Wang, M. G. Sendeku, J. Wang, N. Li, Y. Yao, X. Yang, C. Shan, T. Yang, J. He, *Adv. Funct. Mater.* **2019**, 1902890.

[17] X. Xiong, J. Kang, Q. Hu, C. Gu, T. Gao, X. Li, Y. Wu, *Adv. Funct. Mater.* **2020**, *30*, 1909645.

[18] E. Linardy, M. Trushin, K. Watanabe, T. Taniguchi, G. Eda, *Adv. Mater.* **2020**, *32*, 2001543.

[19] F. Wang, J. Liu, W. Huang, R. Cheng, L. Yin, J. Wang, M. G. Sendeku, Y. Zhang, X. Zhan, C. Shan, Z. Wang, J. He, *Sci. Bull.* **2020**, *65*, 1444.

[20] Z. Lin, B. R. Carvalho, E. Kahn, R. Lv, R. Rao, H. Terrones, M. A. Pimenta, M. Terrones, *2D Mater.* **2016**, *3*, 022002.

[21] Q. Liang, Q. Zhang, J. Gou, T. Song, Arramel, H. Chen, M. Yang, S. X. Lim, Q. Wang, R. Zhu, N. Yakovlev, S. C. Tan, W. Zhang, K. S. Novoselov, A. T. S. Wee, *ACS Nano* **2020**, *14*, 5668.

[22] T. Ahmed, S. Kuriakose, S. Abbas, M. J. S. Spencer, M. A. Rahman, M. Tahir, Y. Lu, P. Sonar, V. Bansal, M. Bhaskaran, S. Sriram, S. Walia, *Adv. Funct. Mater.* **2019**, *29*, 1901991.

[23] Y. Wang, F. Wu, X. Liu, J. Lin, J. Y. Chen, W. W. Wu, J. Wei, Y. Liu, Q. Liu, L. Liao, *Appl. Phys. Lett.* **2019**, *115*, 193503.

[24] A. Ziletti, A. Carvalho, D. K. Campbell, D. F. Coker, A. C. Neto, *Phys. Rev. Lett.* **2015**, *114*, 046801.

[25] C. Xie, P. You, Z. Liu, L. Li, F. Yan, *Light: Sci. Appl.* **2017**, *6*, 17023.

[26] F. H. Koppens, T. Mueller, P. Avouris, A. C. Ferrari, M. S. Vitiello, M. Polini, *Nat. Nanotechnol.* **2014**, *9*, 780.

[27] L. Ye, H. Li, Z. Chen, J. Xu, *ACS Photonics* **2016**, *3*, 692.

[28] C. Xie, C. Mak, X. Tao, F. Yan, *Adv. Funct. Mater.* **2017**, *27*, 1603886.

[29] X. Liu, L. Gu, Q. Zhang, J. Wu, Y. Long, Z. Fan, *Nat. Commun.* **2014**, *5*, 4007.

[30] X. Wang, Z. Cheng, K. Xu, H. K. Tsang, J.-B. Xu, *Nat. Photonics* **2013**, *7*, 888.

[31] X. Qiu, X. Yu, S. Yuan, Y. Gao, X. Liu, Y. Xu, D. Yang, *Adv. Opt. Mater.* **2018**, *6*, 1700638.

**ADVANCED
SCIENCE NEWS**

www.advancedsciencenews.com

**ADVANCED
FUNCTIONAL
MATERIALS**

www.afm-journal.de

[32] D. Lee, E. Hwang, Y. Lee, Y. Choi, J. S. Kim, S. Lee, J. H. Cho, *Adv. Mater.* **2016**, *28*, 9196.

[33] M. V. Konnik, E. A. Manykin, S. N. Starikov, *Opt. Mem. Neural Networks* **2009**, *18*, 61.

[34] P. Giannozzi, O. Andreussi, T. Brumme, P. Giannozzi, O. Andreussi, T. Brumme, O. Bunau, M. Buongiorno Nardelli, M. Calandra, R. Car, C. Cavazzoni, D. Ceresoli, M. Cococcioni, N. Colonna, I. Carnimeo, A. Dal Corso, S. De Gironcoli, P. Delugas, R. A. Distasio, A. Ferretti, A. Floris, G. Fratesi, G. Fugallo, R. Gebauer, U. Gerstmann, F. Giustino, T. Gorni, J. Jia, M. Kawamura, H. Y. Ko, A. Kokalj, E. Küçükbenli, M. Lazzeri, M. Marsili, N. Marzari, F. Mauri, N. L. Nguyen, H. V. Nguyen, A. Otero-De-La-Roza, L. Paulatto, S. Poncé, D. Rocca, R. Sabatini, B. Santra, M. Schlipf, A. P. Seitsonen, A. Smogunov, I. Timrov, T. Thonhauser, P. Umari, N. Vast, X. Wu, S. Baroni, *J. Phys. Condens. Matter* **2017**, *29*, 465901.

[35] Y. H. Cao, J. T. Bai, H. J. Feng, *Chin. Phys. Lett.* **2020**, *1037*, 107301.

[36] P. Bolshakov, C. M. Smyth, A. Khosravi, P. Zhao, P. K. Hurley, C. L. Hinkle, R. M. Wallace, C. D. Young, *ACS Appl. Electron. Mater.* **2019**, *1*, 210.

[37] Y. Lv, Q. Tong, Y. Liu, L. Li, S. Chang, W. Zhu, C. Jiang, L. Liao, *Phys. Rev. Appl.* **2019**, *12*, 044064.

[38] R. L. Kumawat, B. Pathak, *Appl. Surf. Sci.* **2020**, *529*, 147094.